Dylan Johnston | 1003852690
Nikhil Narayanan | 1000448465
Hassan Masoudi | 1003746280

Final Design Report
Talon Agricultural Drone

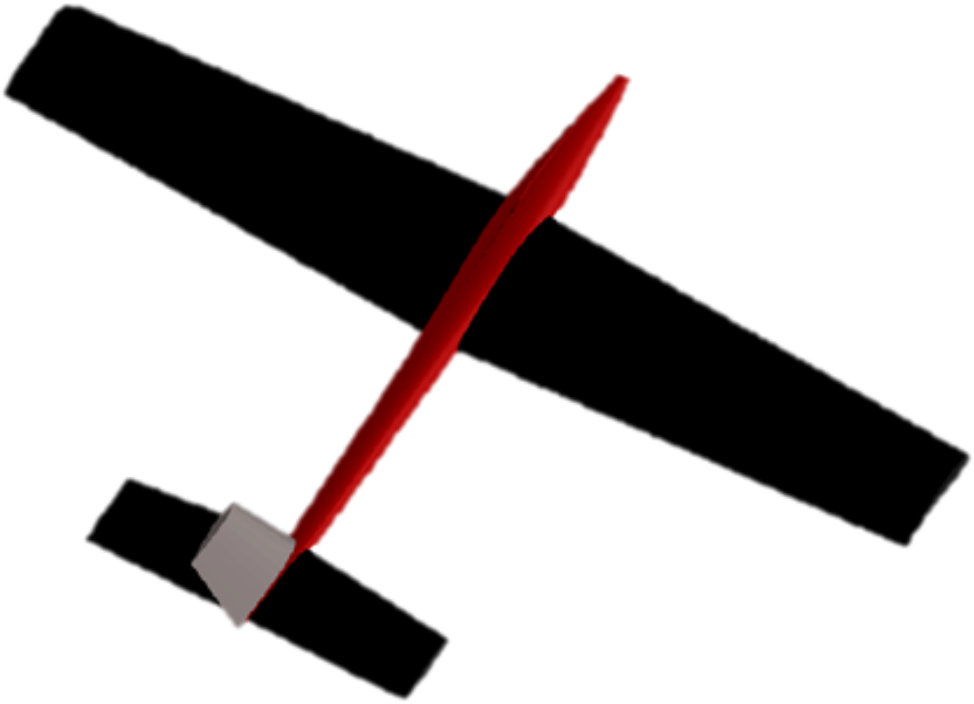

AER 1216 | Fundamentals of UAV Design
UTIAS | University of Toronto
Thursday December 21st, 2017

Abstract

The final design of the Talon agricultural UAV is presented, along with performance, stress, and stability analyses. Final design considerations, including construction materials, stress analyses, dynamic stability mode analyses, control surface performance, a cost analysis, and final payload selection are explained including all assumptions that were used in their derivation. Preliminary design considerations are summarized and presented.

Contents

List of Figures

List of Tables

1 Goal and Design Objectives

The goal of this project is to design a commercial unmanned aerial vehicle for agricultural crop inspection. The vehicle must be able to resolve spots on plants 7 millimeters in diameter with a minimum of 25 pixels per dot area, and must inspect an area of 250 meters by 250 meters. Navigation and image processing are considered beyond the scope of this project, with emphasis placed instead upon maximizing image quality and aeronautical performance. There are no limitations placed on the cost of the vehicle, however cost should be minimized in order to compete in the commercial agricultural drone market.

The chosen drone configuration was fixed wing. This configuration was chosen to allow for higher cruise speeds and longer flight endurances and ranges. This allows the UAV to cover larger distances in less time. This in turn improves the image qualities, allowing for consistent lighting over the duration of the mission, as well as a reduction in noise in the image. Finally, the flight of the drone will be less impacted by environmental conditions such as higher wind velocities.

With the intention of creating a viable and competitive product, this design aims to complete the mission objectives in a single flight, without the need to land for any reason until inspection of the area is complete. The drone will be designed for longevity and reliability, with an expectation that it will be employed on a weekly basis, in ideal or near ideal flight and image capture conditions. The design aims to make the product portable by minimizing the vehicle size, while increasing practicality and robustness by including support for alternative image capturing techniques. Emphasis is placed on optimizing aeronautical performance in terms of the vehicle's lift to drag ratio.

2 Mission Design

2.1 Camera Analysis

The primary design constraint for the given mission objective is the selection of camera. The cruising altitude of the drone will be limited by the resolution and field of view of the camera chosen, while cruising speed will be limited by the frame rate and shutter speed. A minimum resolution of 25 pixels per 7 millimeter diameter dot was used to determine a maximum cruising altitude for a number of vertical and horizontal fields of view. The maximum cruising altitude possible to achieve the minimum resolution is given by:

$$h = \sqrt{\frac{A_{dot} R}{4 \tan \frac{\theta_x}{2} \tan \frac{\theta_y}{2}}}$$

Where R is the resolution of the camera in pixels, A_{dot} is the area of the spots we are trying to resolve in meters, and θ_x & θ_y are the horizontal and vertical fields of view respectively. Using this relation, a variety of camera resolutions and fields of view were plotted as a function of height above the crops (Figure 1).

Figure 1 demonstrates that, without the use of a lens, the maximum viable cruising altitude that still facilitates the resolution requirement is approximately 6 meters above the crops. However, it is unreasonable to assume that the drone will not deviate from its cruising altitude during the duration its flight. A cruising altitude of 5 meters was chosen in order to achieve the required resolution in case of any such deviations.

Based on these calculations, a 16 megapixel camera with a horizontal field of view of 50 degrees was chosen. For a cruising altitude of 5 meters, this corresponds to a mapping of approximately 5.6 meters of crop in the horizontal direction, and approximately 4 meters in the vertical direction. The horizontal mapping dictates how many passes across the field must be made for a complete survey, which in turn places requirements on the endurance and range of the drone. In order to relieve endurance requirements, the decision was made to include a second camera directly adjacent to the first camera. Each camera is tilted at a slight angle such that they have a slight overlap directly underneath the drone, but effectively double the horizontal area mapped beneath the drone. Instead of a combined field of view of 100° and a horizontal mapping length of 11.2 meters, an overlap of 0.15 meters directly beneath the drone was chosen. The corresponding field of view of 95.6 ° and a horizontal mapping length of 11.05m. The tilt angle of each camera was calculated using the following expression:

$$\theta_{tilt} = \frac{\theta_x}{2} - \arctan hx$$

Where x is the amount of ground in meters that is covered by overlap directly beneath the drone at an altitude of 5 meters. Including this overlap, as well as an overlap at the edge of either camera's field of view,

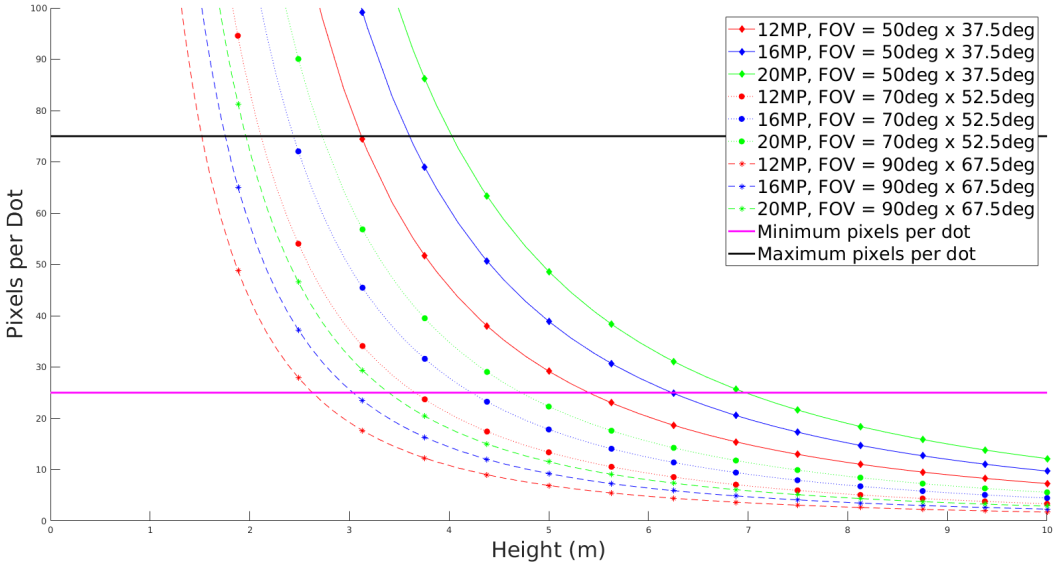

Figure 1: Camera Resolution versus Cruising Altitude

this camera configuration results in a horizontal mapping of approximately 11 meters. This is the width we will use when considering how many passes we will require the drone to make over the field.

The vertical mapping, on the other hand, dictates the maximum speed at which the drone can fly while still achieving a complete survey. The camera chosen achieves a maximum of 60 frames per second, however for higher resolution photos, this number drops closer to 30 frames per second. Using a conservative frame rate of 10 frames per second, the maximum feasible flight speed while still achieving a vertical overlap of approximately 25 percent, is given by:

$$v_{max} = f * \Delta x$$

where f is the frame rate in frames per second and Δx is the maximum distance we would like to fly in meters before taking another photo. Therefore, conservatively, we will need to limit our flight speed to a maximum of 30 meters per second. This will be the upper limit on our cruise velocity, which will is expected to be much closer to 15 $\frac{\text{m}}{\text{s}}$.

A summary of the camera specifications is presented in the below table:

Camera Specification	
FoV	95.6°
Frame Rate	30 FPS
Horizontal Ground Covered	11.05 meters
Resolution	16MP

Table 1: Summary of Camera Specifications

2.2 Flight Path

The flight path of the UAV was determined using the camera properties chosen during camera analysis. With the ability to image 11 meters in the horizontal direction flying at a height of 5 meters, the 250 meter length field is divided up into flight lanes. Each lane is 8 meters in width, with 1.5 meters overlap for each lane. This results in a total of 31 lanes, and a flight range of 7.75 kilometers flying in at cruise conditions.

The aircraft will need to complete a 180° arc after completion of each pass across the field. The turning radius of the aircraft is given by:

$$r = \frac{V^2}{g\sqrt{N^2 - 1}}$$

Where V is the speed of the aircraft in meters per second and N is the integer number of g forces experienced by the craft. For estimated turning flight velocity of 14 meters per second, the corresponding turning radius is 8 meters at 5 g, which translates into a 24 meter arc after each pass across the field. Since there are 32 passes across the field, this corresponds to 31 turns in total, resulting in a total flight range of just under 8.5 kilometers.

An image of a hypothetical flight plan is presented below, along with a summary table for the flight path.

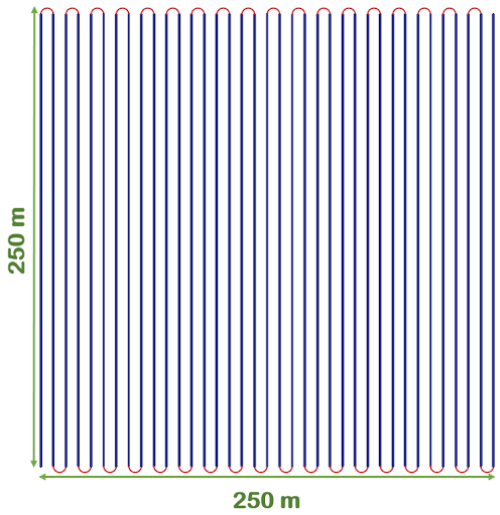

Figure 2: Hypothetical flight plan of the Talon Agricultural UAV over the target field.

Flight Path	
Number of Passes	32
Cruising Speed	17 $\frac{meters}{second}$
Turning Radius	4 meters
Wing Loading	5
Turning Speed	14 $\frac{meters}{second}$
Range	8400 meters

Table 2: Summary of Proposed Flight Path

3 Structural Design and Stress Analysis

3.1 Wing Structure

Based on an estimate preliminary mass budget found in Appendix B, the lift requirement in cruising condition was determined to be 3.7 kilograms for the entire airframe. This number was estimated using an cursory dimensional analysis, literature review, and past experience in constructing a fixed wing UAV. In accordance with the design methodology, the wing span was limited to a maximum of 2 meters in order to retain portability and convenience. An initial aspect ratio of 6 was chosen based on literature aspect ratio values for similar designs and was deemed an appropriate value upon consulting the professor. A initial cruise speed of 12 meters per second was chosen due to it being approximately 30% of our calculated maximum flight speed and therefore certain to retain the desired image quality.

In addition, the following design process was used in the sizing and optimization of the wing geometry. The initial cruise speed, preliminary mass budget and geometrical constraints were used to provide an initial sizing of the aircraft.

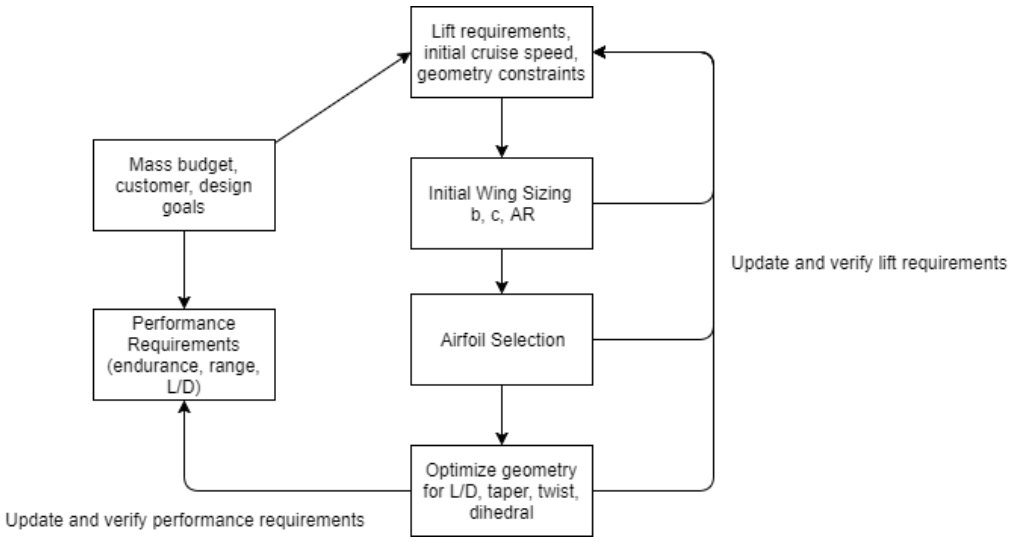

Figure 3: Wing Design Process

3.1.1 Planform Sizing

Given the lift force required by the preliminary mass budget, an initial rectangular wing was sized. An initial lift coefficient value of 1 was chosen and the cruise condition lift equals weight was enforced to calculate the required planform surface area:

$$L = \frac{1}{2} C_L \rho V^2 S = W \Rightarrow S = \frac{2W}{\rho V^2 C_L}$$

$$\therefore S = \frac{2(3.7kg)}{(1.225\frac{kg}{m^3})(12\frac{m}{s})^2(1)} = 0.419m^2$$

The initial aspect ratio requirement, and the corresponding initial cord length, are given below:

$$AR = \frac{b^2}{S} = 6 \Rightarrow b < 1.6m \qquad \therefore c = \frac{S}{b} = 0.264m$$

The initial rectangular planform shape is illustrated in Figure 4 below.

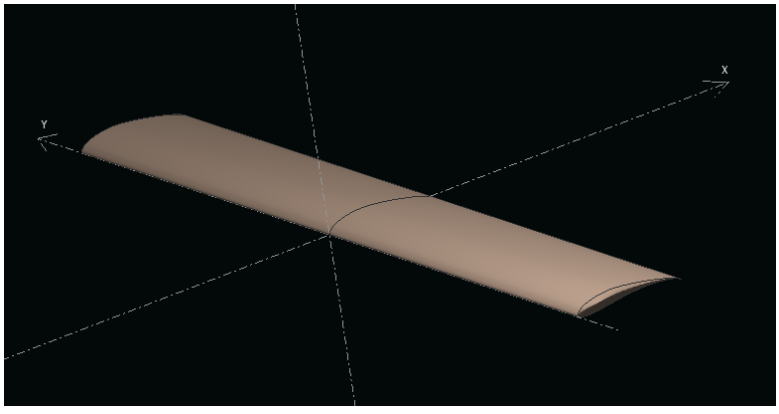

Figure 4: Initial Rectangular Wing Design

3.1.2 Airfoil Selection

At this stage in the design the wing meets the lift and geometry requirements. The next stage is to select an airfoil. In order to maximize the lift to drag ratio at a low Reynold's number, several Selig airfoils were compared and considered for use. The airfoils were analyzed using XFLR5, varying the angle of attack from -5 degrees to 10 degrees and the Reynolds number from 2×10^5 to 4×10^5. The profile for these airfoils, their lift coefficients versus angle of attack and their L/D ratios versus angle of attack were provided in the preliminary

design report. The wing surface selected is the highly cambered S1210 NACA airfoil, and its corresponding previously mentioned figures are given below.

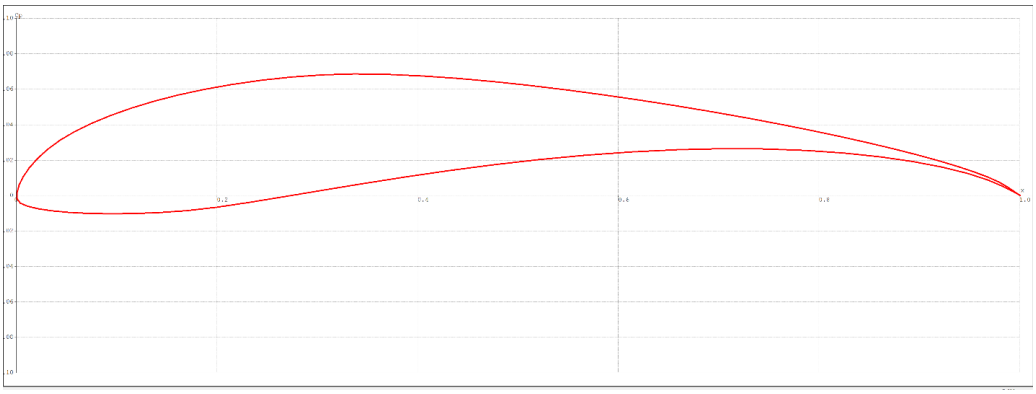

Figure 5: S1210 Airfoil: Profile

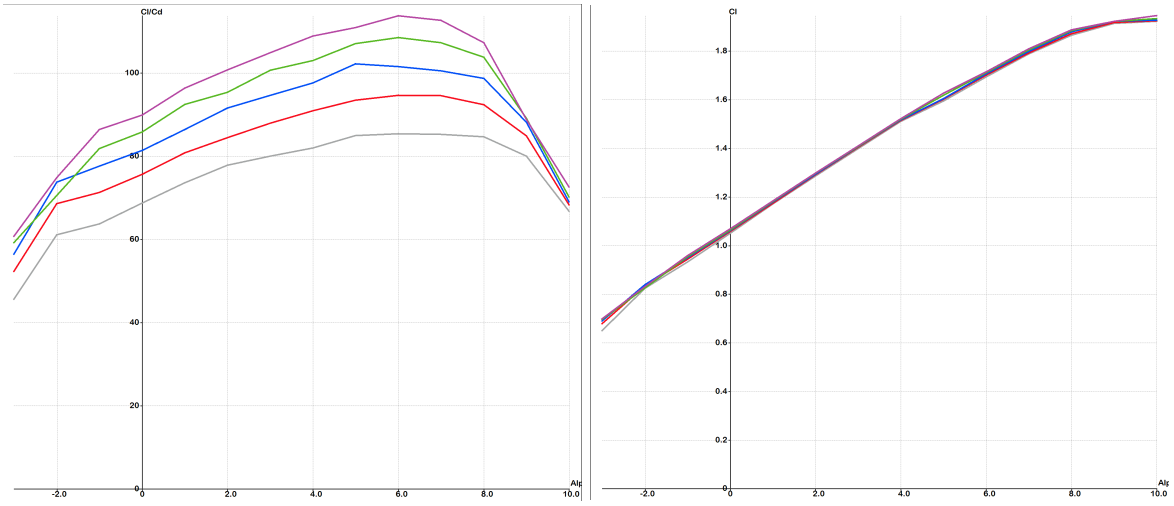

(a) Lift to Drag Ratio vs α

(b) Lift Coefficient vs α

Figure 6: L/D vs α and C_L vs α for the NACA S1210 Airfoil

The S1210 airfoil was chosen based on the lift to drag ratio it achieves at the proposed cruise speed. Additionally, it is a highly cambered airfoil, and thus can be placed at nearly 0° angle of incidence.

3.1.3 Planform Geometry Optimization

Both the taper and the twist of the wing were varied for the chosen planform and airfoil. The intention of this variation was to optimize the wing's lift to drag ratio.

A lifting line theory analysis was performed on the wing using XFLR5, for a taper ratio ranging from 0 to 0.8. It should be noted that the analysis provided by this program only considers wing structure, and ignores any effects due to the fuselage, tail, and interference effects.

The trade offs between improved lift distribution and increased total drag were considered. As the taper ratio increased from 0 to 0.8, the lift distribution along the wing tended towards an ellipse. An elliptical lift distribution results in a near constant downwash across the span and thereby a minimization in induced drag. The resulting increase in L/D was found to peak at a taper ratio of 0.58, with larger taper ratios resulting in an aspect ratio approaching a value of 8. In order to maintain our desired aspect ratio, while still improving our L/D, a taper ratio of 0.7 was included in our wing geometry. The relation between the wing's L/D ratio at the chosen cruise velocity for a number of tapers is shown in Figure 7.

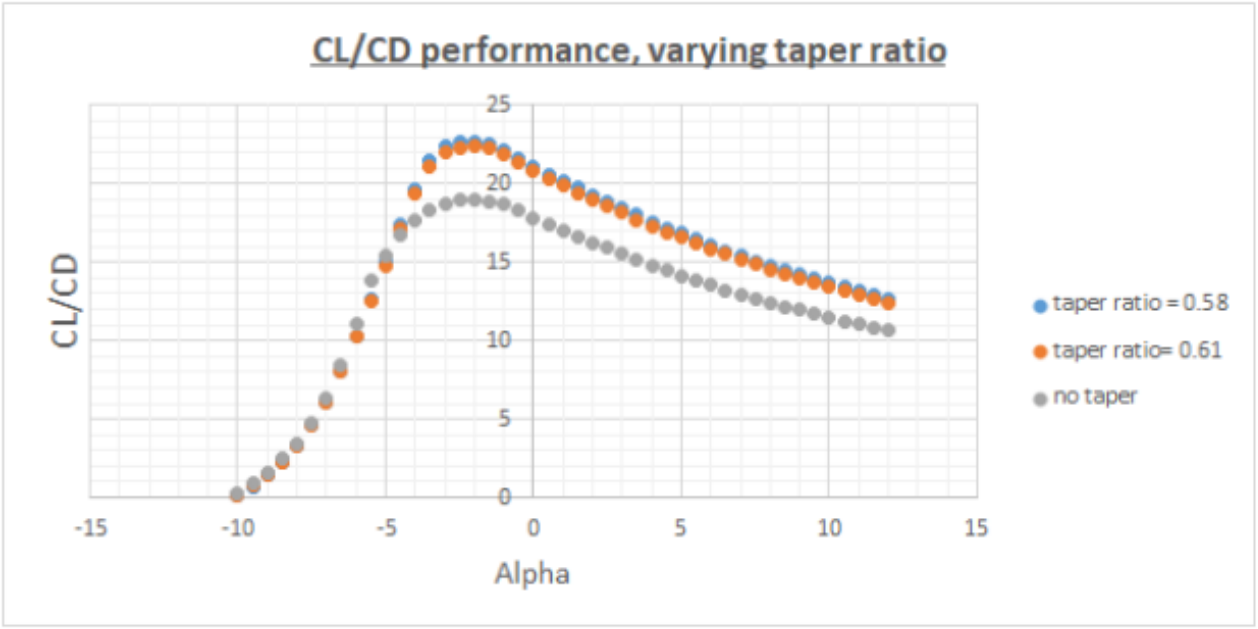

Figure 7: Variation in C_L/C_D performance with taper

A similar twist analysis was performed, with the intention to adjust the wingtip to be at a lower angle of attack than the chord, and thus prevent tip stall. The trade off between increased drag and increased performance at stall inducing orientations (roll or steep climbs) was considered, and a 3° twist was included in the wing geometry. While the twist does not improve the aircraft's L/D ratio, it allows the aircraft to retain roll control at a wider variety of flight orientations.

The L/D ratio versus angle of attack for the final wing geometry is provided in Figure 8. The characteristics of the planform are summarized in Table 3.

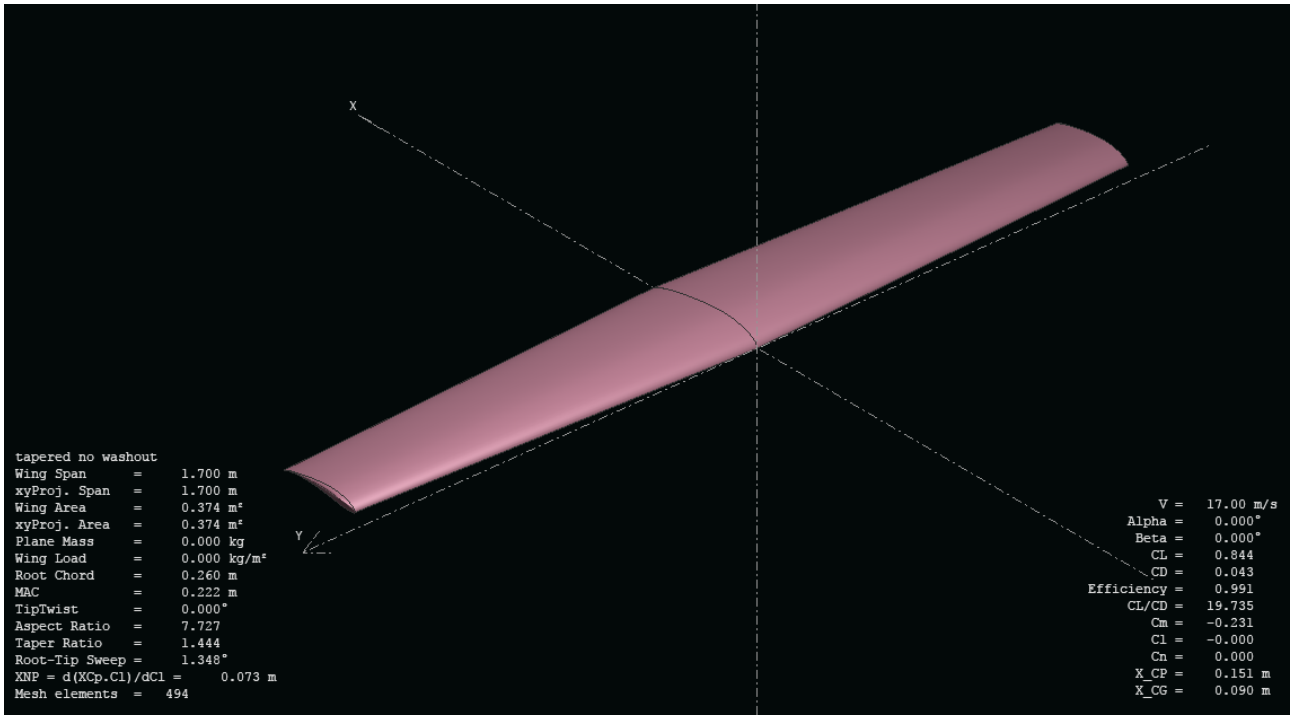

Figure 8: Final Wing Geometry

Planform Specification	
Span	1700 millimeters
Mean Chord	220 millimeters
Airfoil	NACA 1210
Twist	3°
Taper	0.7

Table 3: Final Planform Geometry Specifications

The L/D ratio with varying angle of attack for the final wing is plotted in Figure 9.

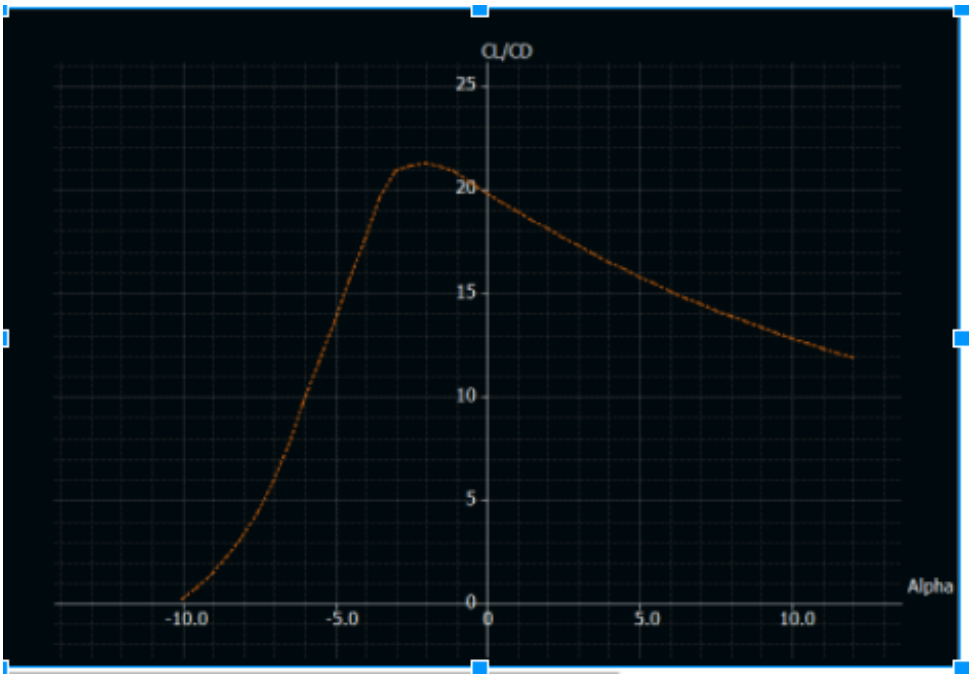

Figure 9: CL/CD performance for the twisted and tapered wing

3.1.4 Control Surface Sizing

The control surfaces were sized according to common literature values. The decision to not include a rudder was made with the intention to give the UAV a high yaw stiffness, C_{N_β}, and rely on the elevators for turning control of the UAV. This decision will not largely affect the yaw control of the UAV, since a single propeller is being used for propulsion, thus removing the possibility of asymmetric thrust. Additionally, the assumed flight conditions will not have significant enough resulting side slip complications to destabilize the aircraft. There is a risk of a resulting unstable dutch roll mode, but upon dynamic stability analysis, this was not an issue.

The ailerons were chosen to be 25% of the cord length of the wing based on literature values. The ailerons were offset from the tip of the wing by 10% of the half span of the wing, in order to insure that roll control is maintained in the even of tip stall. Each aileron has a length of $\frac{1}{4}$ of the wing span.

The aileron dimensions, as well the total hinge moment, are summarized in the table below.

Aileron Specifications	
Span	435 millimeters
Mean Chord	49 millimeters
Hinge Moment	0.0013 $\frac{kgm^2}{s^2}$

Table 4: Summary of Aileron Specifications

3.1.5 Wing Materials

The proposed wing geometry consists of the following elements:

- **Balsa and Ply Wood Ribs** - The wing planform will consist of 20 ribs made of two 2.5 millimeter thick ply wood airfoil profile layered on either side of a 1 millimeter thick balsa wood airfoil profile. The intention of the balsa wood is to reduce some weight of the aircraft, while plywood is chosen for its superior stiffness. Additional weight may be removed by removing a section of the airfoil profile, at the cost of reduced bending strength.
- **Carbon Fiber Spars** - Two cylindrical carbon fiber spars will extend along the length of the aircraft, each 1460 millimeters in length and 20 millimeters in diameter. The primary purpose of these spars is to resist lateral stress due to lift of the wing. These spars will connect every rib via cylindrical holes which will be cut into each airfoil profile.
- **Ply Wood Trailing and Leading Edge Reinforcements** - A 10 millimeter wide and 3 millimeter thick rectangular prism of plywood will be included at the leading edge of the wing, to provide increased bending stress distribution along the wing, and at the trailing edge of the wing, to reinforce the thin trailing edge of the airfoil.
- **Balsa Wood Surface** - A 1.6 millimeter thick Balsa wood surface will cover the entire wing. Balsa wood was chosen due to its low density and therefore low weight, which will allow the planform to retain the shape of the airfoil without an increased weight.
- **XPS Foam** - The ailerons of the wing will be made of XPS foam due to their lack of moisture absorption, and low weight.
- **Monocoat** - A monocoat layer will cover the entire planform to ensure a smooth surface and decrease the skin friction of the wing.
- **Adhesive** - Structural adhesive will be used to hold all of the structural elements of the plane together.

A 2-dimensional CAD of the proposed wing geometry is provided below, with the ribs indicated in purple, the Spars in blue, the ailerons in green, and the surface in white.

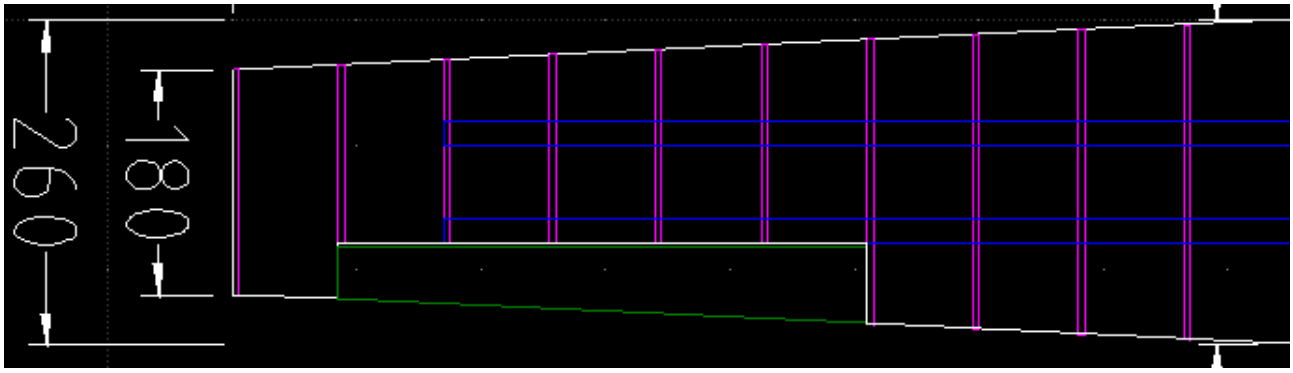

Figure 10: 2-Dimensional CAD Drawing of Wing Structure

3.1.6 Wing Stress Analysis

A simple engineering beam analysis was done on the primary wing structure i.e. the carbon fiber spar in the maximum loading case. This maximum load was taken to be a load factor of 5 in addition to the self weight of the wing. A load factor 5 will likely occur only the worst case turning or pitching scenarios. We do both a worst case bending and torsion analysis cases.

The load on the wing will be the sum of the following:

$$P = 5(L - W_{wing})$$

Which will act throughout the wing as a function of the lift distribution across the wing. The span lift distribution (non dimensionalized) is presented in Figure 11

The non dimensional C_l given by the wing was converted into a dimensional span wise lift by:

$$L/span = C_l q \bar{c}$$

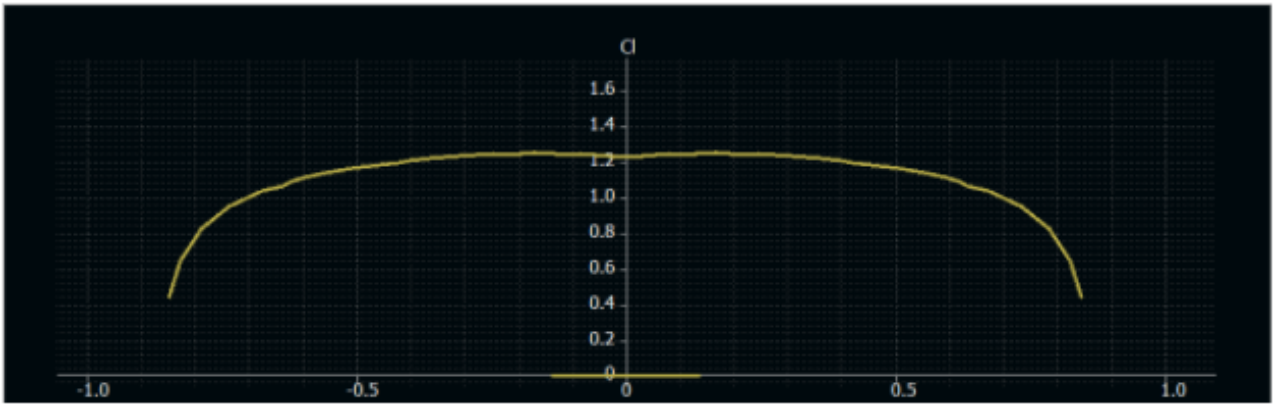

Figure 11: Spanwise Lift Distribution

The weight per unit span from the wing structure was determined by the material composition of the wing structure as presented in the previous section. Based on adding up all the masses per unit span of the wing structural components we get a weight per unit span of **2.78N/m**.

Using the discrete lift distribution above, a fourth order polynomial was fit to get a continuous spanwise lift distribution, V(x). We subtract off the weight per unit span acting in the opposite direction:

$$V(x) = (1.17 + 1.148x - 8.44x^2 + 16.8x^3 - 11.8x^4 - 2.78)q\bar{c}$$

Using the Euler-Bernoulli beam equation we get the following 4th order equation which we can integrate to obtain the stresses and deflections. Note that the maximum stresses will occur at the root of the spar and the maximum deflection will occur at the tip.

$$\frac{d^4w}{dx^4} = \frac{5}{EI}(1.17 + 1.148^x - 8.44x^2 + 16.8x^3 - 11.8x^4)q\bar{c}$$

Table 5: Structural Characteristics of Spanwise Main Spar

Maximum deflection (m)	0.005
Maximum Stress (Pa)	3.67×10^6
Yield Stress (Pa)	3.5×10^9

We also do a worst-case torsional analysis on a rib by applying a moment of 2Nm on the rib and analyzing the angle of rotation. A unit torque is the worst case loading scenario (5xload factor applied). This torque will be the total lift of the wing divided by the total number of ribs. This not a precise assumption but it will suffice to determine the strength of the ribs. The total lift on the wing will be 30N, and given there are 20 ribs there will be 1.5N acting on a single rib in the z direction. We will assume this 1.5N acts in pure torsion of the cross sectional rib and add in a factor of safety of 1.5 to apply 2N of pure torsional force on the rib.

The rib is modeled as a rectangular cross section with thickness 0.005m and length 0.22m and height 0.026m. The torsion is applied longitudinally. Given a torsional constant GJ = 8.8e5 we can find the effect of a unit torque.

$$\theta = \frac{TL}{GJ} = 2.8582e - 3degrees$$

Thus the rotations of the rib are very small. In addition we also calculate the shear stresses on a particular rib section due to a unit torque.

$$\tau = \frac{T\rho}{J} = 17.11MPa$$

The yield strength is 48MPa, so there is a factor of safety of 2.8 in this loading scenario and the rib will not fracture. In addition the design of the rib is well within structural loading limits.

3.2 Tail Structure

3.2.1 Horizontal Stabilizer Sizing

The initial horizontal tail volume was chosen based on an MIT aircraft sizing guideline. The volume was chosen to be 0.5 cubic meters. This value was chosen from the higher end of the spectrum, since a larger horizontal tail volume will provide increased pitch stiffness, and therefore increased longitudinal stability for the aircraft while it is imaging the crops. Figure 12 demonstrates the effect of horizontal tail volume on pitch stiffness, which is calculated using the following equation:

$$C_{m_\alpha} = a_{total} K - \bar{V_H} a_t$$

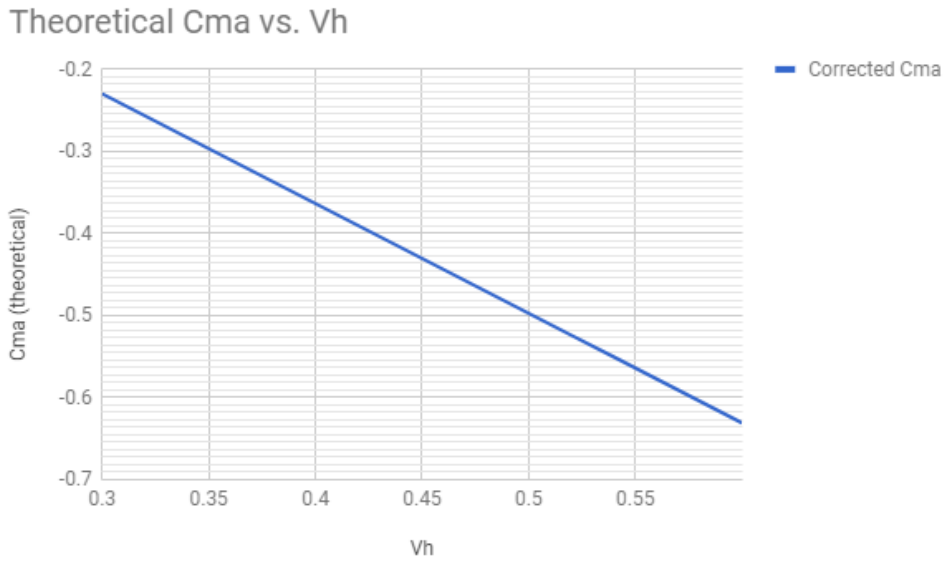

Figure 12: C_M versus Horizontal Tail Volume

Where K is the static margin, and a_{total} and a_t are the lift slopes of the total aircraft and the tail respectively. A pitch stiffness of -0.5 corresponds to the chosen tail volume, which relatively high, and provides the aircraft with a superior longitudinal static stability.

Using the chosen tail volume, the moment arm and surface area of the horizontal tail were varied, while keeping their product constant, according to the following equation:

$$S_h I_h = \bar{V_h} \cdot S \cdot \bar{c}$$

The trade off between horizontal stabilizer surface area and moment arm was considered. A surface area of horizontal stabilizer equal to approximately 20% of the wing was chosen, which requires a moment arm of approximately 700 millimeters. This value was chosen using the MIT aircraft sizing guideline, along with a desire to control the length of the fuselage, and the static margin. The dimensions of the horizontal stabilizer are summarized in Table 6.

Horizontal Tail Specifications	
Span	600 millimeters
Mean Chord	135 millimeters
Horizontal Tail Volume	0.5 m^3
Taper Ratio	0.7
Aspect Ratio	4.44
Surface Area	0.085 m^2
Moment Arm	700 millimeters

Table 6: Summary of the Horizontal Tail Dimensions

The characteristics of the horizontal stabilizer provided by XFLR5 are provided in Table 7.

Horizontal Tail Characteristics	
C_{m_α}	-0.71
C_{m_0}	0.05
α_{trim}	2.5 °

Table 7: Summary of the Horizontal Tail Characteristics

3.2.2 Vertical Stabilizer Sizing

The vertical stabilizer was chosen using a similar process to that of the horizontal stabilizer. The following formula was used to decide on ratio of surface area to moment arm:

$$S_v I_v = \bar{V_v} \cdot S \cdot b$$

Since our planned configuration dictated that the location of the horizontal stabilizer be adjacent to the vertical stabilizer, we chose the same moment arm, determined the surface area via the above equation. The dimensions of the vertical stabilizer are summarized in Table 8.

Vertical Tail Specifications	
Height	502 millimeters
Mean Chord	135 millimeters
Vertical Tail Volume	0.5 m^3
Sweep	14
Aspect Ratio	3.72
Surface Area	0.04 m^2
Moment Arm	700 millimeters

Table 8: Summary of the Vertical Tail Dimensions

A render of the complete tail can be seen in Figure 13 below.

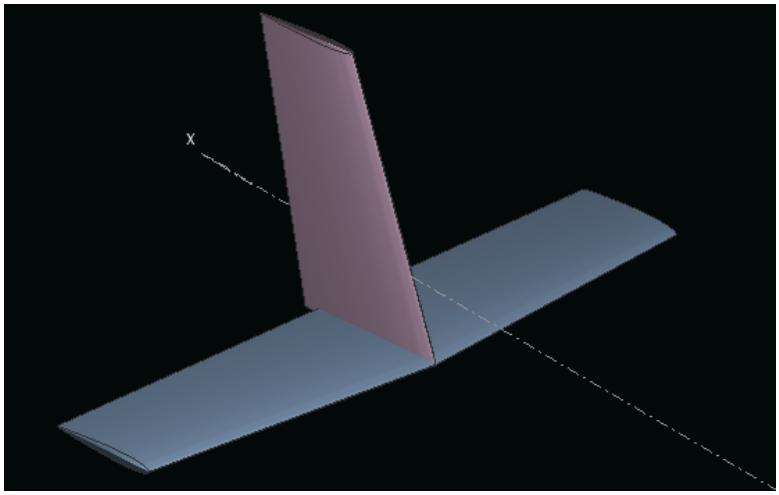

Figure 13: Final Tail Design without Elevators

3.2.3 Control Surface Sizing

The elevators were chosen to have a width of 25% of the root chord, and to extend along the entire span of the horizontal stabilizer. The intention of this geometry is to provide the UAV with superior pitch control, allowing the UAV to remain within a meter of the proposed 5 meter cruise altitude. A summary of the elevator characteristics, and their respective hinge moment, is provided in Table 9.

Vertical Tail Specifications	
Span	600 millimeters
Mean Chord	33.75 millimeters
Hinge Moment	$1.74 \times 10^{-4} \frac{kgm^2}{s^2}$

Table 9: Summary of Elevator Specifications

3.2.4 Tail Materials

The proposed tail geometry consists of the following elements:

- **XPS Foam** - The horizontal and vertical stabilizer planforms, as well as the elevators, will be made of XPS foam due to their lack of moisture absorption and low weight.

3.3 Fuselage Structure

3.3.1 Fuselage Dimensions

Fuselage length is usually chosen to be approximately 75% of the wingspan in order to maintain a certain pitch stiffness. Our design chose to use larger horizontal stabilizers to retain pitch stiffness, while decreasing the moment arm in an attempt to reduce aircraft weight. The decision was made to restrict the length of the fuselage to approximately 65% of the wingspan.

The geometry of the fuselage was chosen to be cylindrical for the sections in contact with planforms, namely the wing and tail, and conical for the remainder of the vehicle, with the intention of reducing parasite drag and form drag. Both the preliminary battery and camera configuration chosen for the UAV necessitated a fuselage diameter of at least 80 millimeters. In order to provide some extra space, a fuselage diameter of approximately 15% of the wingspan, or 100 millimeters, was decided upon. A 2-dimensional CAD rendering of the fuselage can be seen in Figure 14.

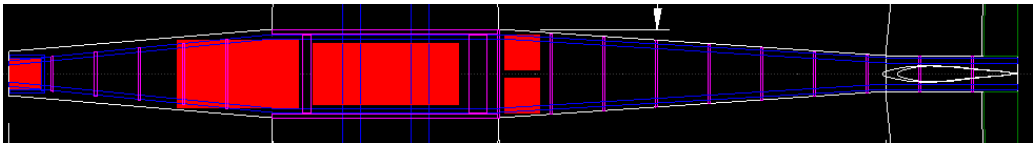

Figure 14: 2-Dimensional CAD rendering of Fuselage

Help Fill This In

Fuselage Dimensions	
Length	1150 millimeters
Nose Cone Tip Diameter	50 millimeters
Nose Cone Base Diameter	100 millimeters
Nose Cone Length	300 millimeters
Wing Cylinder Diameter	100 millimeters
Wing Cylinder Length	260 millimeters
Tail Cone Tip Diameter	40 millimeters
Tail Cone Base Diameter	100 millimeters
Tail Cone Length	440 millimeters
Tail Cylinder Diameter	40 millimeters
Tail Cylinder Length	150 millimeters

Table 10: Summary of Fuselage Dimensions

A Solidworks rendering of the fuselage shell is provided below.

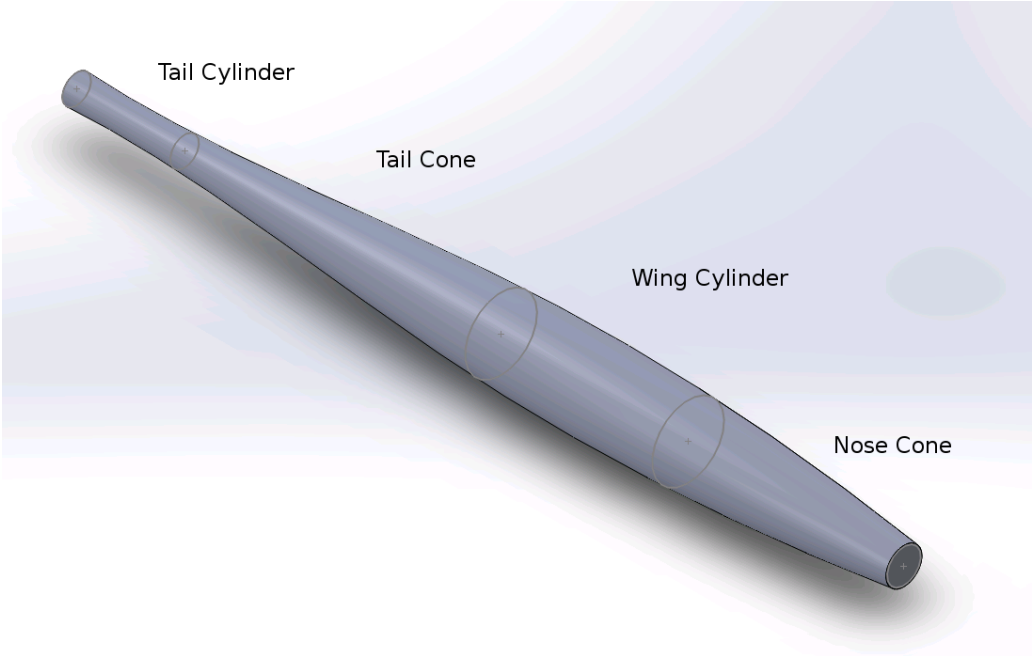

Figure 15: 3-Dimensional SolidWorks rendering of Fuselage

3.3.2 Payload Placement

Our planned aircraft configuration was a tractor orientation, with the propeller positioned at the nose of the aircraft. The intention was to place the battery as close as possible to the center of gravity, since it was the heaviest element. By putting the heaviest element close to the center of gravity of the aircraft, the center of gravity could be offset by including ballast in the front or aft of the aircraft, to allow for different payloads (for example alternative imaging hardware or alternative integrated autopilots). The battery is placed below the wing spars, since a lower center of gravity results in a positive roll stiffness, acting to reduce the roll of the aircraft from unexpected rolling movements.

It was decided that the cameras should be located near the center of gravity, so that pitch deviations would not affect image quality. Additionally, since the battery would need to be removed for charging, and the cameras would need to be removed for charging and to obtain the images, placing the battery and cameras beside one another allowed for their access via a single panel, reducing the number of removable parts on the aircraft fuselage.

Since the selected cameras have their own battery power, it was decided that the autopilot should also be located in the nose of the vehicle, so that the motor and autopilot were in close proximity, and so that the only wiring directed towards the tail of the aircraft would be for elevator control.

The payload placement can be seen in Figure 14.

3.3.3 Landing Gear

A tricycle configuration was chosen based on literature review, with one wheel located near the nose of the vehicle, and two wheels located on either side of the fuselage. This allows for steerable control on the ground, reduced stress on the nose during landing, and a symmetrical weight distribution. A commercial landing gear was chosen, with the the nose wheel located 150 millimeters in front of the leading edge, and the two additional wheels located 50 millimeters behind the center of gravity. These positions ensure that the aircraft does not tip during landing, and that the propeller is raised sufficiently off the ground to avoid damage during landing. The nose wheel was chosen to have a vertical height of 250 millimeters, at an angle of 15 ° with to the normal direction of the runway. This allows for approximately 100 millimeters of clearance for the propeller, and allows the wheel some room for bending upon landing, instead of a strict compression force. Similarly, the aft wheels were chosen to have a vertical height of 200 millimeters, and an angle of 5 degrees with respect to the normal direction of the runway to allow for similar stress modes.

3.3.4 Fuselage Materials

The chosen fuselage geometry was composed of the following structural elements:

- **Carbon Fiber Spars** - 4 carbon fiber spars run along the length of the fuselage. In the nose, tail cone, and tail cylinder sections, these spars are oriented at 45° from the vertical axis of the aircraft in order to provide relief from longitudinal bending. In the wing cylinder, these spars are adjusted to be oriented at 60° from the vertical axis of the aircraft in order to allow for the battery to be removed from the fuselage. Carbon fiber was chosen due to its light weight and resistance to bending.
- **Ply Wood Ribs** - 15 ply wood ribs run along the length of the fuselage, along with 2 thicker ply wood ribs located in the wing cylinder. These ribs are circular in shape, and have holes cut in them to allow the carbon fiber spars to connect them together in a cohesive shape. These spars allow for a rigid shape of the aircraft, and provide contact points for the spars. The two thicker ply wood ribs are included near the aircraft's center of gravity since there will be the most stress on the spars at these locations. Ply wood was chosen due to its strength and relatively low weight.
- **Ply Wood Wing Spar Interface** - A sheet of ply wood is located on either side of the wing cylinder to allow for the wing spars and fuselage spars to connect at a single interface. This aids in the distribution of the lift force over the entire aircraft.
- **Balsa Surface** - The entire fuselage, similar to the wing, is surface using balsa wood. This allows for the aircraft to retain its shape during flight, while remaining relatively low weight due to the low density of balsa wood.
- **Monocoat** - The balsa wood surface is coated in monocoat to reduce skin friction of the fuselage.
- **Structural Adhesive** - A structural adhesive is used to connect the elements of the aircraft due to its light weight.

3.3.5 Fuselage Access Points

A single access point is included on the bottom of the fuselage, allowing for access to the cameras and battery for recharging purposes.

3.4 Assembly

The assembly of the Talon Agricultural drone is completed in the following steps upon receiving the product:

- The fuselage comes in tact, complete with motor and integrated autopilot. The wings are divided into two halves, each with one wing spar anchored firmly in the wing. The tail comes in three sections: each half of the horizontal stabilizer and the vertical stabilizer. The landing gear is not attached when shipped
- The wings are inserted through the cavities in the sides of the fuselage, running through the slots in the ply wood spar interface, and through into the adjacent wing. The wing spars are then locked in place via the fuselage access point.
- The vertical and horizontal stabilizers are attached at their respective locations.
- The wheels are attached at their respective locations, anchored firmly into the large plywood rib in the wing cylinder and a spar connector in the nose.

After charging the battery and cameras, an initial systems check should be performed on the integrated autopilot, the motor and the servos connected to the control surfaces.

4 Part Selection

4.1 Battery Selection

Current drones on the market were analyzed. It was decided that a major complaint was the battery life of drones, requiring frequent charging or additional batteries for continued operation. In this vein, a large battery with a charge rating of 8000 milliamp hours. This allows for an extended flight time, enabling the Talon agricultural drone to achieve longer mission requirements, or unexpected flight conditions. The properties of the chosen battery are summarized in Table 12.

Table 11: Battery Properties

Name	ZIPPY Flightmax 8000mAh
Capacity (mAh)	8000
Mass (g)	845

Table 12: Specifications of Chosen Battery

4.2 Motor Selection

The motor was selected based on the weight, maximum flight velocity, maximum battery voltage, and a desired power/weight value of 175 Watts/kg. This results in a desired Motor power of approximately 387 Watts.

Since maximum power loading occurs under static conditions, power and thrust calculations done at zero airspeed will satisfy the motor not-to-exceed conditions for any airspeed. Thus, the power of the propeller can be calculated using the following equations:

$$P_{prop} = C_p \cdot \rho \cdot n^3 \cdot D^5$$
$$T_{prop} = C_t \cdot \rho \cdot n^2 \cdot D^4$$

Next we match the motor Kv rating and battery voltage. This can be done by approximating the revolution rate as:

$$RevRate = \frac{V_{max}}{(0.2 \cdot D) + (0.74 \cdot p)}$$

And then calculating the Kv rating of the motor using:

$$Kv = \frac{(RevRate \cdot 60)}{V_{batt}}$$

So the resulting Kv rating we require is 450 rpm/V, and the required power is approximately 380 Watts. The motor selected is the Turnigy L3537-840 Brushless motor, which has a Kv rating of 840 rpm/V and a power rating of 380 Watts. The properties of the selected motor are summarized in Table 14.

Table 13: Motor Properties

K_v	840 rpm/V
Max Power	340
Mass	117
Max Current	30 A
Voltage	14.8 V

Table 14: Specifications of Chosen Motor

4.3 Propeller Selection

The above motor selection was performed assuming a propellor of diameter 11 inches and pitch of 6 inches. The chosen propeller is the Aerostar Composite propeller, which has the above dimensions.

5 Performance Analysis

5.1 Center of Mass

Matlab was used to sum over all of the components of the aircraft, along with their longitudinal distances from the leading edge of the trailing edge (axial symmetry was assumed). The Matlab script used to perform this calculation is provided in the appendix. The resulting total mass of the aircraft weighs in at 2.5 kg (including an adjustment for weight of epoxy) with the center of mass located 102 millimeters from the leading edge. Since the neutral point was found to be 138 millimeters from the leading edge of the aircraft, the UAV was found to

have a static margin of 16%. The finalized mass budget is provided in Table 15, with the mass of the constituent structural elements amalgamated into a single entity.

UAV Component	**Mass (kg)**
Battery	0.845
Motor	0.117
Propeller	0.036
Integrated Autopilot	0.413
Camera	2×0.073
Wing	0.457
Tail	0.075
Fuselage	0.25
Landing Gear	0.3

Table 15: Finalized Mass Budget for Talon Agricultural Drone

5.2 Drag Estimation

Two methods were used to calculate the total drag on the aircraft. Assuming that drag is composed of a combination of the parasite (zero-lift) drag and the induced drag, a drag polar was estimated using both theoretical methods and a XFLR5 VLM simulation on the lifting surfaces. Empirical and simulated values were compared in order to gauge the quality of the simulation, so that synthesized estimate could be derived.

5.2.1 Empirical Drag Estimation

Raymer (1992) provides the following estimation for all the parasite drag components of the aircraft.

$$\sum_{c=1}^{n} C_{f_c} F F_c Q_c \frac{S_{wet}}{S} + C_{D_L}$$

The following table presents the estimates for each of the components of the aircraft.

Surface	**Friction Factor**	Q factor	Cf	S_{wet}/S_{ref}	Product
Wing	0.9139	1.2	0.00240	2.06	0.00542
H-stab	1.104	1.04	0.003182	0.4373	0.00159
V-stab	0.9409	1.04	0.003183	0.2186	0.000681
Fuselage	1.160	1	0.001423	0.1146	0.0001894

Margin Factor	2
Total CD0	0.016

The details of finding Q, FF and Sw can be found in literature. The key assumption is that the flow is primarily laminar, and the margin factor of 2 accounts for the transition into the turbulent region at some critical location on the wing. In addition, the margin is used to partially account for interference drag between the fuselage and wing joints.

The empirical estimation of induced drag is given by:

$$C_{D_i} = \frac{1}{\pi e AR} C_L^2$$

We are given the wing geometry and need to find the Oswald efficiency factor e, a derivation of which can also be found in the reference noted above. The value was found to be 0.86 using equation 13.26 in chapter 13. The induced drag factor, K, has a value of 0.0480. An expression for the drag polar is given by:

$$C_D = 0.0161 + 0.0480 C_L^2$$

5.2.2 Simulated Estimate (XFLR5)

A 3D VLM, viscous simulation of the aircraft at a cruising velocity of 19 meters per second was performed on XFLR5 for just the lifting surfaces (wing and tail) in order to obtain the drag polar shown in Figure 16.

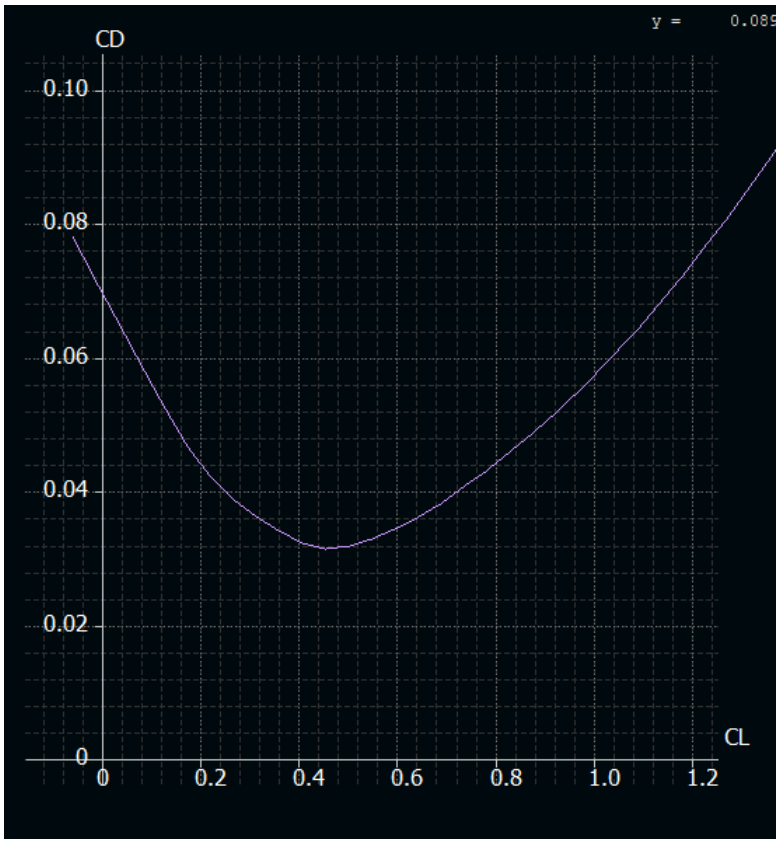

Figure 16: Drag Polar For Lifting Surfaces

From the simulation, a C_{d_0} value of 0.069 and an induced drag component of 0.07 were determined. An important note is that this simulation does not take into account viscous or interference effects from the fuselage. Additionally, the analysis is done using a 2-dimensional drag for lifting surfaces, which cannot be interpolated to 3-dimensions. Adding in a theoretical fuselage viscous drag estimate of 0.00018, a total C_{d_0} of 0.0691 was found.

The simulated values were found to be dramatically higher, in particular the parasite drag component. It was noted by our group that this value was likely much to high, and possibly a pessimistic result. A value between the two drag calculations was chosen, due to flaws in the empirical calculation and limitations in the simulated estimation. The C_{D_0} was expected to be closer to 0.03, so this is the value we will use in the analysis of range, endurance and thrust.

Our drag polar is then:

$$C_D = 0.03 + 0.07C_L^2$$

5.3 L/D Analysis

The simulated lift to drag ratio of the aircraft maximizes around an angle of attack of 1 degree. Given the trim condition is at around 3 degrees, the lift to drag ratio remains close to its maximum value of 18. It is important to note that this is an overestimation from the VLM simulation on XFLR5. From the simulation, a maximum L/D of around 17.5 is expected. An overestimation factor of 1.2 will be included (based on the XFLR5 literature) to give us a final predicted lift to drag ratio at cruise of 15.

5.4 Cruise Condition Analysis

The lift slope curve for the aircraft is presented in Figure 17.

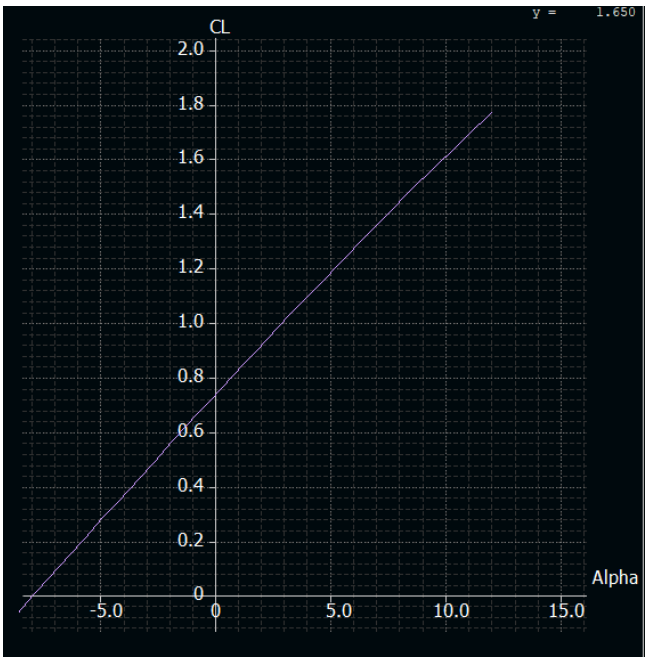

Figure 17: Lift Slope for the entire aircraft

From the lift slope and trim conditions, and using the cruise velocity of 17 m/s, the C_L at cruise will be 0.9, but accounting for the overestimation from XFLR5 we divide this by 1.2 to get a cruise C_L of 0.75. The simulation failed to converge past an angle of attack of 13 degrees, so at this stage we will take this as stall angle of attack. This corresponds to a $C_L = 1.75$, which is corrected to a value of $C_L = 1.45$. The stall velocity is then given by:

$$V_{stall} = \sqrt{\frac{2L}{C_L \rho S}} = 10.5 m/s$$

In addition our motor selection provides more than the required thrust at both stall conditions and at cruise conditions. This implies that the aircraft will have a high climb rate upon take off and at low speed. Therefore, we can conclude that the aircraft will have sufficient power to stay in the air at cruise, as well as an additional thrust capacity available for use during non ideal flight conditions.

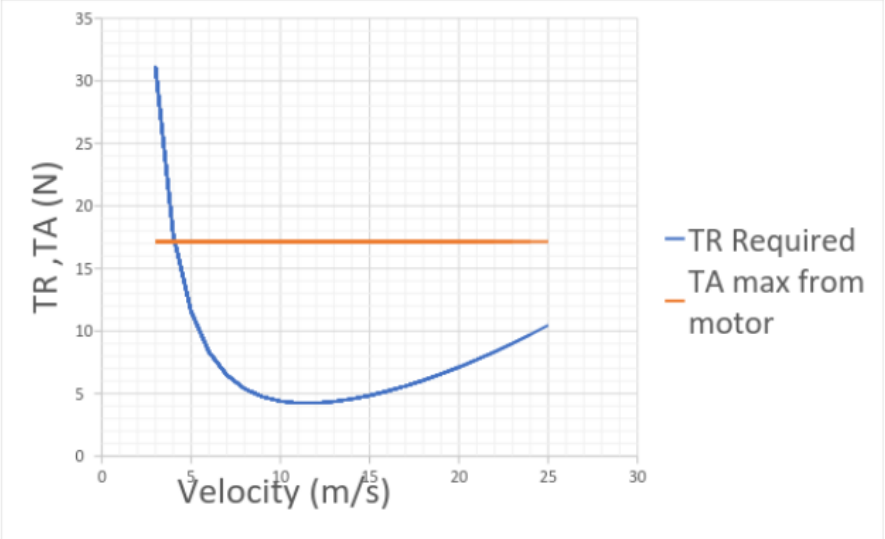

Figure 18: Thrust Required and Thrust Available at various velocities

Figure 18 demonstrates that the available thrust from the selected engine is 17.15 Newtons. This UAV is designed to fly at a velocity of 17 m/s, which, according to the graph, requires a thrust of 5.6 N to remain at

cruise. Since the drone will ideally be used in normal flight conditions, this engine will provide both endurance and performance, with extra thrust available should the flying conditions deteriorate.

Using the online software motocalc, optimal thrust requires a 11 inch diameter and 6 inch pitch propeller.

5.5 Range and Endurance Analysis

Following the lift to drag performance we analyze the performance of the endurance parameter for a propeller driven aircraft in XFLR5. This is illustrated in Figure 19 below:

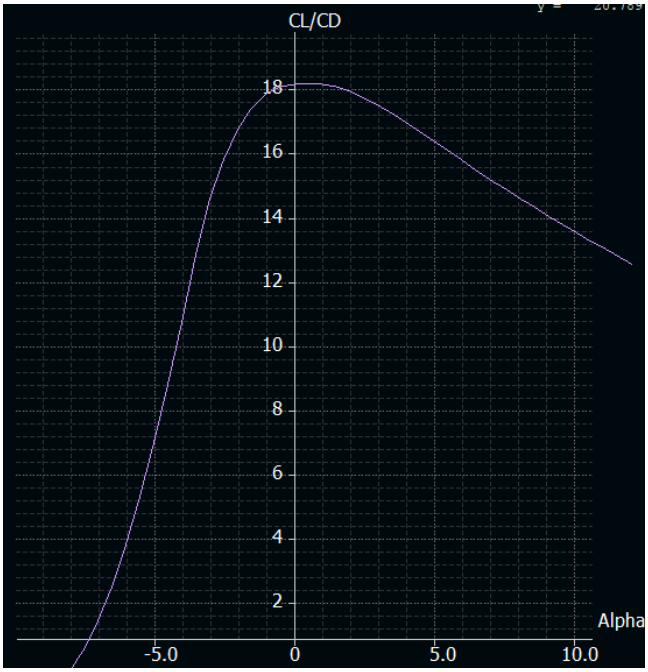

Figure 19: C_L/C_D performance

The aircraft's endurance achieves a maximum at a L/D ratio of 17.5 and at an angle of attack of 5 degrees.

The range and endurance of the aircraft will be dictated by the performance of the battery and motor. The endurance that the 8000mAh battery can provide the chosen motor is given by the following expression:

$$8(Ah) \times 14.8V = 118.4Wh = 426240J$$

$$E = \frac{426240}{95.2} = 4477.3seconds = 74.5minutes$$

Note that this is not taking into account servo actuation or the powering of the integrated autopilot. Adjusting for both of these factors, the estimated endurance is closer to 60 minutes.

The linear range of the aircraft for this endurance is simply the endurance multiplied by the flight velocity, resulting in a range of just over 60 kilometers, however, functionally, the range will be smaller due to considerations such as accelerating and maneuvering.

5.6 Take Off Analysis

The following equation was integrated to calculate the take off distance of the aircraft:

$$D_{takeoff} = \int \frac{V^2 \cdot m \cdot dV}{2(T(V) - D(V) - (\mu_r(W - L(V))))}$$

Where the value for thrust required at a given velocity was calculated using MotoCalc. The drag used was a combination of the rotational kinetic friction of the wheels on the runway surface (assumed to be gravel) and the aerodynamic drag of the aircraft itself. Assuming we need a takeoff velocity approximately 20% greater than stall speed, the resulting take off distance is approximately 16 meters.

6 Stability Analysis

6.1 Static Stability

After sizing the wing and tail sections, a static stability analysis of the aircraft was performed. Specifically highlighted are the high pitch stiffness and yaw stiffness of the aircraft.

The static stability of the aircraft is summarized in the table below. Note that the values are generated from an XFLR5 viscous, VLM method analysis on only the wing and tail configuration. The addition of fuselage will add to the longitudinal pitch stiffness.

Stability Derivative	**Value**
$C_{m\alpha}$	-0.717
$C_{n\beta}$	0.206
C_{lp}	-0.484
Neutral Point (m)	0.138

The relatively high pitch roll and yaw stiffnesses indicate that the aircraft will perform well in off design conditions. For example if there are large wind gusts during operations, the high stiffnesses will stabilize the aircraft, so that adequate images can be taken without a need for a second pass over the field.

The longitudinal stability curve is presented in Figure below. Note that the aircraft attains trim at an angle of attack of approximately 3 degrees; this value can be modified by adding elevators as required.

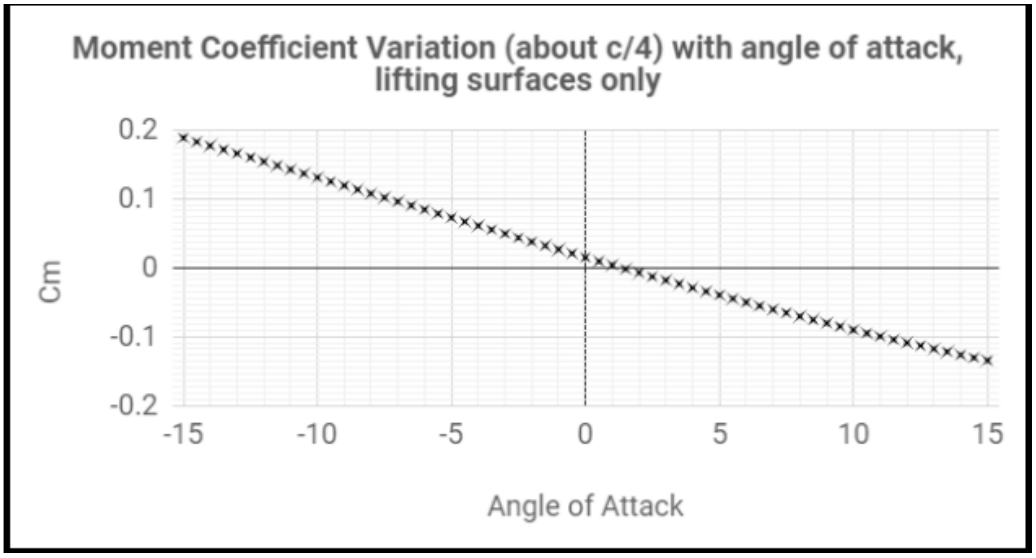

Figure 20: Variation in moment coefficient with angle of attack

6.2 Dynamic Stability Analysis

An inviscid dynamic stability analysis was done on XFLR5 to determine the eigenvalues of lateral and longitudinal modes of the aircraft.

Table 16: Dynamic Modes and Eigenvalues

Dynamic Mode	**Eigenvalues**
Phugoid	$-0.01157 \pm 0.997i$
Short Period	$-12.89 \pm 12.26i$
Dutch Roll	$-3.474 \pm 8.33i$
Spiral Mode	-2.737
Roll Damping	-20.09

All the required eigenvalues are well within the left half plane indicating they have stable dynamic modes.

7 Cost Analysis

An estimated cost budget based on industry prices is provided in Table 21

Name	QTY	Cost	Final Cost
Carbon Fiber Rod	2	$ 10.00	$20.00
Turnigy L3537-840 Brushless Motor (380w)	1	$ 20.00	$20.00
ZIPPY Flightmax 8000mAh 4S1P 30C	1	$ 50.00	$50.00
Turnigy AE-30A Brushless ESC	1	$ 12.00	$12.00
Aerostar Gas Series Wood Propeller 11x6 (1pc)	1	$ 4.00	$4.00
Hinge	5	$ 1.00	$5.00
Control Horn	5	$ 1.00	$5.00
Nylon Clevis	10	$ 0.80	$8.00
Servo	4	$ 4.00	$16.00
Pushrods (10)	1	$ 2.00	$2.00
Autopilot	1	$ 300.00	$300.00
LED light	2	$ 5.00	$10.00
2.4 12 CH RC	1	$ 180.00	$180.00
Balsa	10	$ 15.00	$150.00
Ply	5	$ 20.00	$100.00
Ply rod	5	$ 15.00	$75.00
FOXEER 4K BOX Action Camera w/ WiFi	2	$ 150.00	$300.00
Landing Gear	1	$ 30.00	$30.00
Total			**$1,287.00**

Figure 21: Estimated cost of drone components in USD

References

[1] John David Anderson. *Introduction to Flight.*

[2] A. Depperois. Xflr5 results vs. predictions, 2009.

[3] Bernard Etkin. *Dynamics of Atmospheric Flight.*

[4] MIT Opencourseware. Lab 8 notes: Basic aircraft design sizing rules.

[5] Jan Roskam. *Methods for estimating stability derivatives of conventional subsonic airplanes.*

[6] Lance Traub. Range and endurance estimates for battery-powered aircraft. 48:703–707, 03 2011.

[7] Ugur C Yayli, Cihan Kimet, Anday Duru, Ozgur Cetir, Ugur Torun, Ahmet Aydogan, Sanjeevikumar Padmanaban, and Ahmet H Ertas. Generic aircraft design flowchart. *Small Unmanned Fixed-wing Aircraft Design*, 4(1):65–80, Nov 2017.

8 Appendix

A MatLab Center of Mass Calculation

```
close all
clear all
clc

% Define all required input variables:

% Basic Parameters

g = 9.8;
rhoinf = 1.225;
qmax = 0.5 * rhoinf * 20^2;

% Structural Characteristics

% Masses (kg)

Mbattery = 0.845;
Mengine = 0.117;
Mprop = 0.036;
Mavionics = 0.413;
Mcamera = 2 * 0.0732;
Mlandinggear = 0.10
% Mwing = 0.457;
% Mfuselage = 0.250;

% Structural Dimensions and Masses

% Materials
density_ply = 5*10^-7;
density_balsa = 1.7*10^-7;
density_spar = 2*10^-9;
balsa_thickness = 1.6;

% Wing
number_of_wing_ribs = 22;
area_of_wing_ribs = 5808;
width_balsa_wing_rib = 4;
width_ply_wing_rib = 1;
mean_chord_length = 220;
mean_airfoil_max_thickness = 26.4;
wing_half_span = 850;
length_wing_spar = 1460;
wing_spar_diameter = 20;

% Fuselage
fuselage_rib_1_diameter = 10;
fuselage_rib_2_diameter = 20;
fuselage_rib_diameter = 2.5;
wing_cylinder_diameter = 100;
wing_cylinder_length = 260;
tail_cylinder_diameter = 40;
tail_cylinder_length = 150;
```

```
nose_cone_tip_diameter = 50;
nose_cone_extended_height = 600;
tail_cone_extended_height = 733 + (1/3);
tail_cone_height = 440;

fuselage_spar_diameter = 5;
motor_holster_length = 36;
motor_holster_width = 3.5;
motor_holster_side_length = 39;
motor_holster_side_width = 3.5;
wing_spar_brace_height = 40;


%%%%%%%%%%%%%%%%%%%%%%%%%%%%%%%%%%%%%%%%%%%%%%%%%%%%%%%%%%%%%%%%%%%%%%%%

M_wing_ribs = number_of_wing_ribs * area_of_wing_ribs *
 ((width_balsa_wing_rib * density_balsa) + (width_ply_wing_rib *
 density_ply));
M_wing_balsa_surface = (((mean_chord_length *
 mean_airfoil_max_thickness) - ((mean_chord_length -
 2*balsa_thickness)*(mean_airfoil_max_thickness - 2*balsa_thickness)))
 * wing_half_span / 2) * density_balsa;
M_wing_spar = pi * length_wing_spar * (wing_spar_diameter / 2)^2 *
 density_spar;

Mwing = M_wing_ribs + (2*M_wing_balsa_surface) + (2*M_wing_spar);

%%%%%%%%%%%%%%%%%%%%%%%%%%%%%%%%%%%%%%%%%%%%%%%%%%%%%%%%%%%%%%%%%%%%%%%%

m_fuselage_wing_cylinder_structure = pi*((fuselage_rib_1_diameter /
 2)^2 + (fuselage_rib_2_diameter/2)^2) * wing_cylinder_diameter *
 density_ply;
m_fuselage_tail_cylinder_structure = 8 * pi* (fuselage_rib_diameter /
 2)^2 * tail_cylinder_diameter * density_ply;
m_fuselage_nose_cone_structure = 20 * pi * (fuselage_rib_diameter /
 2)^2 * (wing_cylinder_diameter + nose_cone_tip_diameter)/2 *
 density_ply;
m_fuselage_tail_cone_structure = 32 * pi * (fuselage_rib_diameter /
 2)^2 * (wing_cylinder_diameter + tail_cylinder_diameter)/2 *
 density_ply;

M_fuselage_ply = m_fuselage_wing_cylinder_structure +
 m_fuselage_tail_cylinder_structure + m_fuselage_nose_cone_structure +
 m_fuselage_tail_cone_structure;

%%%%%%%%%%%%%%%%%%%%%%%%%%%%%%%%%%%%%%%%%%%%%%%%%%%%%%%%%%%%%%%%%%%%%%%%
%%%%

m_fuselage_nose_cone_surface = density_balsa * (pi/3) *
 (((wing_cylinder_diameter/2)^2 * nose_cone_extended_height)...
    - (((wing_cylinder_diameter - (2*balsa_thickness))/2)^2 *
 nose_cone_extended_height)...
    - ((((wing_cylinder_diameter / 2) / 2)^2 *
 (nose_cone_extended_height / 2) - ((((wing_cylinder_diameter/2) -
```

```
 2*balsa_thickness)/2)^2 * (nose_cone_extended_height / 2))))); %
 cone of length 600mm - interior cone - (cone of length 300 - interior
 cone)

m_fuselage_tail_cone_surface =  density_balsa * (pi/3) *
 (((wing_cylinder_diameter/2)^2 * tail_cone_extended_height)...
    - (((wing_cylinder_diameter - (2*balsa_thickness))/2)^2 *
 tail_cone_extended_height)...
    - ((((tail_cylinder_diameter / 2) / 2)^2 *
 ((tail_cone_extended_height - tail_cone_height)/ 2) -
 ((((tail_cylinder_diameter/2) - 2*balsa_thickness)/2)^2 *
 ((tail_cone_extended_height - tail_cone_height)/ 2))));

m_fuselage_wing_cylinder_surface = density_balsa* pi *
 wing_cylinder_diameter * wing_cylinder_length * balsa_thickness;
m_fuselage_tail_cylinder_surface = density_balsa * pi *
 tail_cylinder_diameter * tail_cylinder_length * balsa_thickness;

M_fuselage_balsa = m_fuselage_wing_cylinder_surface +
 m_fuselage_tail_cylinder_surface + m_fuselage_nose_cone_surface +
 m_fuselage_tail_cone_surface;

%%%%%%%%%%%%%%%%%%%%%%%%%%%%%%%%%%%%%%%%%%%%%%%%%%%%%%%%%%%%%%%%%%%%%%%%%%%%
%%%%%%%%%%%%%

m_fuselage_spar_nose_cone = (4 * pi*(fuselage_spar_diameter / 2)^2
 * tail_cone_height + (motor_holster_length^2 * motor_holster_width)
 + 2* (motor_holster_side_length^2*motor_holster_side_width)) *
 density_spar;
m_fuselage_spar_tail_cone = 4 * pi*(fuselage_spar_diameter / 2)^2 *
 tail_cone_height * density_spar;
m_fuselage_spar_tail_cylinder = 4 * pi * (fuselage_spar_diameter /
 2)^2 * tail_cylinder_length * density_spar;
m_fuselage_spar_wing_cylinder = ((4*pi*(fuselage_spar_diameter /
 2)^2 * wing_cylinder_length) + (2 * wing_cylinder_length *
 wing_spar_brace_height * fuselage_spar_diameter)) * density_spar;

M_fuselage_spar = m_fuselage_spar_nose_cone +
 m_fuselage_spar_tail_cone + m_fuselage_spar_tail_cylinder +
 m_fuselage_spar_wing_cylinder;

%%%%%%%%%%%%%%%%%%%%%%%%%%%%%%%%%%%%%%%%%%%%%%%%%%%%%%%%%%%%%%%%%%%%%%%%%%%%
%%%%%%%%

Mfuselage = M_fuselage_balsa + M_fuselage_ply + M_fuselage_spar;

%%%%%%%%%%%%%%%%%%%%%%%%%%%%%%%%%%%%%%%%%%%%%%%%%%%%%%%%%%%%%%%%%%%%%%%%%%%%

M_horizontal_stabilizer = 0.045;
M_vertical_stabilizer = 0.030;

Mtail = M_horizontal_stabilizer + M_vertical_stabilizer;
```

```
% %%%%%%%%%%%%%%%%%%%%%%%%%%%%%%%%%%%%%%%%%%%%%%%%%%%%%%%%%%%%%%%%%%%%%%%
%%

Mtotal = Mwing + Mtail + Mfuselage + Mbattery + Mengine + Mprop +
 Mavionics +  Mcamera + 3*Mlandinggear;
W = g * Mtotal;

% Component COM Positions (m)

Rtail = 760;
Rwing = 120;
Rfuselage = 260;
Rbattery = 130;
Rengine = -281.5;
Rprop = -302;
Ravionics = -39;
Railerons = 205;
Relevators = 831.25;
Rcamera = 285;
Rlandinggear1 = -150;
Rlandinggear2 = 152;

% COM Calculation

COM = ((Mwing * Rwing) + (Mtail * Rtail) + (Mfuselage * Rfuselage)...
    + (Mbattery * Rbattery) + (Mengine * Rengine) + (Mprop * Rprop) +
 (Mavionics * Ravionics)...
     + (Mcamera * Rcamera)) + (Mlandinggear * Rlandinggear1) +
 (Mlandinggear * 2 * Rlandinggear2) / Mtotal


% Camera Variables

HFOV = 50;
VFOV = 37.5;
Resolution = 16;
rdot = 0.0035;
Adot = pi * rdot^2;

% Camera Calculations

Pixelsperdot = @(height) Camera(height,Resolution,HFOV,VFOV,Adot);
eta = Camera(6,Resolution,HFOV,VFOV,Adot);
XLOV = Dimension(5,HFOV)
YLOV = Dimension(5,VFOV)

fplot(Pixelsperdot, [0,10])
axis([0,10,0,100])

Dfuselageparasite = Sfuselage * CFViscous * kfuselage
MinThrustRequired = 2 * W * sqrt(K * CD0);
WingLoad = W / Sw;
TRminVel = sqrt(2 * WingLoad / (rhoinf * sqrt(CD0 / K)));
```

```
Tavail = qmax * Sw * CD0 + (W^2) / (qmax * Sw * pi * OswaldEWing *
 ARw);
```

```
Mlandinggear =

    0.1000
```

```
COM =

  202.1194
```

```
Undefined function 'Camera' for input arguments of type 'double'.

Error in UAVCalculations (line 156)
eta = Camera(6,Resolution,HFOV,VFOV,Adot);
```

Published with MATLAB® R2017b